Title
Mapping the self-generated magnetic fields due to thermal Weibel instability

Journal
Proceedings of the National Academy of Sciences of the United States of America, 119(50)

ISSN
0027-8424

Authors
Zhang, Chaojie
Wu, Yipeng
Sinclair, Mitchell
et al.

Publication Date
2022-12-13

DOI
10.1073/pnas.2211713119

Peer reviewed

PNAS RESEARCH ARTICLE | PHYSICS OPEN ACCESS

Mapping the self-generated magnetic fields due to thermal Weibel instability

Chaojie Zhang[a,1], Yipeng Wu[a,1], Mitchell Sinclair[a], Audrey Farrell[a], Kenneth A. Marsh[a], Irina Petrushina[b], Navid Vafaei-Najafabadi[b,c], Apurva Gaikwad[b], Rotem Kupfer[c], Karl Kusche[c], Mikhail Fedurin[c], Igor Pogorelsky[c], Mikhail Polyanskiy[c], Chen-Kang Huang[d], Jianfei Hua[e], Wei Lu[e], Warren B. Mori[a,f], and Chan Joshi[a,1]

Edited by Neta Bahcall, Princeton University, Princeton, NJ; received July 10, 2022; accepted October 18, 2022

The origin of the seed magnetic field that is amplified by the galactic dynamo is an open question in plasma astrophysics. Aside from primordial sources and the Biermann battery mechanism, plasma instabilities have also been proposed as a possible source of seed magnetic fields. Among them, thermal Weibel instability driven by temperature anisotropy has attracted broad interests due to its ubiquity in both laboratory and astrophysical plasmas. However, this instability has been challenging to measure in a stationary terrestrial plasma because of the difficulty in preparing such a velocity distribution. Here, we use picosecond laser ionization of hydrogen gas to initialize such an electron distribution function. We record the 2D evolution of the magnetic field associated with the Weibel instability by imaging the deflections of a relativistic electron beam with a picosecond temporal duration and show that the measured *k*-resolved growth rates of the instability validate kinetic theory. Concurrently, self-organization of microscopic plasma currents is observed to amplify the current modulation magnitude that converts up to ~1% of the plasma thermal energy into magnetic energy, thus supporting the notion that the magnetic field induced by the Weibel instability may be able to provide a seed for the galactic dynamo.

Weibel instability | optical-field ionization | temperature anisotropy | self-magnetization | kinetic theory

Observations suggest that ~μG-level magnetic fields exist in all galaxies and the more rarefied intergalactic medium (1–3). At present, these magnetic fields are thought to arise from the amplification of "seed" fields by galactic dynamo (4–6) whereby the kinetic energy of plasma flows is converted into magnetic field energy via induction. The origin of such seeds, however, is still not well understood. Primordial magnetic fields could have been generated during inflation and cosmological phase transitions before recombination and structure formation (7). Apart from these possibilities, astrophysicists have also invoked the Biermann battery effect (6–9) arising from nonparallel density and temperature gradients in plasmas to explain the origin of the seed magnetic field, while acknowledging that the seed fields could also arise from plasma kinetic instabilities including Weibel instability (10–16) that grows due to electron temperature anisotropy. Unlike the Biermann battery mechanism that produces macroscopic fields, Weibel instability grows rapidly and generates magnetic fields on kinetic scales ($\sim c/\omega_p$), raising the concern on their significance for galactic scale fields. Recent theoretical and simulation results suggest that the correlation length of the Weibel magnetic field grows rapidly with time, thus drastically suppressing diffusive dissipation and enabling the field to survive on cosmological timescales (15–17). While there have been some laboratory laser–plasma experiments that purport to show that the protogalactic seed magnetic fields may be due to the Biermann battery process (9), and other experiments that have shown that magnetic fields can be generated by the ion Weibel instability in interpenetrating laser-produced plasmas (18–20), there has been no experimental proof of the generation of magnetic fields because of the electron Weibel instability arising from the temperature anisotropy (subject of this work).

First theorized six decades ago, Weibel instability is arguably the earliest discovered plasma kinetic instability and yet its conclusive experimental verification has proven to be very challenging for two primary reasons. First, until recently, it had not been possible to generate a plasma with a known temperature anisotropy as initially envisioned by Weibel (10). Second, there was no suitable technique to measure the complex and evolving topology of the ultrafast (e.g., on the picosecond time scale in laser-produced plasmas) magnetic fields generated in the plasma. This is particularly the case for the electron Weibel instability because of its generally faster growth rate and shorter wavelength originating from the much smaller inertia of electrons compared to ions.

Significance

Weibel instability driven by temperature anisotropy is thought to be an important mechanism for self-magnetization of many laboratory and astrophysical plasmas, yet its unambiguous demonstration remains a challenge. This work employs an experimental platform that allows us to "design" highly anisotropic electron velocity distributions using optical-field ionization of hydrogen gas and measure the subsequent self-organization of plasma currents and magnetic fields driven by Weibel instability with unprecedented spatiotemporal resolution using ultrafast electron probing. As the plasma thermalizes, a significant amount of electron energy is converted into magnetic energy, which supports the hypothesis that the Weibel instability may provide the seed that is amplified by the galactic dynamo to produce microgauss-level magnetic fields that exist in the cosmos.

Author contributions: C.Z. and C.J. designed research; C.Z., Y.W., M.S., A.F., K.A.M., I. Petrushina, N.V.-N., A.G., R.K., K.K., M.F., I. Pogorelsky, and M.P. performed research; C.-K.H., J.H., W.L., and W.B.M. contributed new reagents/analytic tools; C.Z. and C.J. analyzed data; and C.Z. and C.J. wrote the paper.

The authors declare no competing interest.

This article is a PNAS Direct Submission.

[1]To whom correspondence may be addressed. Email: chaojiez@ucla.edu, wuyipeng@ucla.edu, or cjoshi@ucla.edu.

This article contains supporting information online at https://www.pnas.org/lookup/suppl/doi:10.1073/pnas.2211713119/-/DCSupplemental.

Published December 5, 2022.

Since its discovery, extensive theoretical studies and particle-in-cell (PIC) simulations have revealed important characteristics of Weibel magnetic fields (21–23). For instance, it is predicted that the Weibel instability in an infinite plasma initially grows with a broad k-spectrum, $0 < k < \sqrt{A}\omega_p/c$, where k is the wavenumber of the magnetic field, $A \equiv \frac{T_{\rm hot}}{T_{\rm cold}} - 1$ the temperature anisotropy of the plasma, ω_p the plasma frequency, and c the speed of light in vacuum. $T_{\rm hot}$ and $T_{\rm cold}$ are temperatures in the two orthogonal directions. The broad spectrum implies that many modes are excited simultaneously–each mode having an effective growth rate. As the temperature anisotropy decreases, the k-spectrum is expected to shrink to a narrow peak (23). Physically, the narrowing of the k-spectrum is caused by the coalescence of plasma currents accompanied by the amplification of the magnetic fields. Once the quasi-single mode is formed, the magnetic field can maintain its topological structure for many plasma periods ($\gg \omega_p^{-1}$). Although most theoretical treatments assume a temperature anisotropy in two dimensions, plasma produced by the electric field of an ultrashort laser pulse may have different temperatures along all the three Cartesian coordinates, which leads to the growth of multidimensional Weibel instability. It is crucial to experimentally demonstrate this evolution of the k-spectrum of the magnetic field to conclusively attribute it to the Weibel instability. To our knowledge, this has not been done before.

It is well known that numerous kinetic instabilities–so called because they arise due to nonthermal (non-Maxwellian) and/or anisotropic velocity distribution functions of electrons and/or ions–can be self-excited in plasmas. These instabilities can be predominantly electrostatic/longitudinal, electromagnetic/transverse, or a mixture of the two. We have previously shown that optical-field ionized (OFI) plasmas produced by intense femtosecond laser pulses are an excellent platform for studying this class of instabilities because uniform underdense plasmas with extremely high ($A \gg 10$) and predictable temperature anisotropies can be formed during the ionization process itself (24–26). In previous works, we have documented the onset, saturation, and evolution of the streaming (electrostatic) and oblique current filamentation (electromagnetic with electrostatic components) instabilities by measuring the density fluctuations associated with them by Thomson scattering using a femtosecond probe pulse (25). Furthermore, in a recent experiment, we have confirmed the existence of the quasi-static magnetic field directly by measuring the deflection of a relativistic electron probe beam (27). The final topology of the magnetic field was consistent with that due to the Weibel instability. However, in that experiment, measurement of the onset and the subsequent evolution of the k-spectrum of the magnetic field, required to definitively attribute the phenomenon as a manifestation of the Weibel instability, was not possible.

Other previous work on the Weibel instability has involved the streaming of two counterpropagating laser-produced solid target plasmas (18, 20, 28). In such cases, the Weibel instability arises from the filamentation of the ions on a much longer timescale (typically on nanosecond timescale). One could call this a Weibel-type instability (11) because such a configuration too gives rise to a filamentary magnetic field in the overlap region of the two plasmas but it is not the scenario envisioned by Weibel, where the instability arises from the temperature anisotropy of a stationary plasma (10). Attempts to control beam–plasma parameters more precisely were made in experiments where well-characterized electron beams from linear accelerators were sent through plasmas to study the relativistic current filamentation instability (CFI) (29). The electron bunch was observed to form filamentary structures after its passage through the plasma. Similar behaviors of the electron bunch were also observed in experiments using ultrashort electron bunches from laser wakefield accelerators (30). The study of CFI has also been extended to the overdense plasma regime in relativistic laser–or beam–solid interactions (31–36). Recent studies show that in the case of dilute beam, the dominant mode is oblique (22, 37).

In this article, we show the measurements of Weibel-generated magnetic fields in plasmas produced by ultrashort but intense, linearly polarized CO_2 laser pulses via optical-field ionization. We begin by producing anisotropic OFI hydrogen plasmas by using picosecond CO_2 laser pulses and then using ultrashort relativistic electron bunches from a linear accelerator to probe the magnetic fields. A movie of the magnetic fields with an exposure of ~ps and frame separation from a few to a few tens of ps was made using the electron beam probe. Analysis of the individual frames reveals how the k-spectrum and magnitude of the magnetic fields evolve as a function of time, with micron-level spatial resolution, and thus allows us to validate the predictions of the Weibel theory.

Results

Deflection of the Probe Beam by Self-Generated Magnetic Fields in the Plasma. The experiment was performed at the Accelerator Test Facility of Brookhaven National Laboratory (ATF-BNL). The experimental layout is sketched in Fig. 1*A*. Anisotropic underdense plasmas [$n_e \approx (1.8 \pm 0.2) \times 10^{18}\,{\rm cm}^{-3}$] were created by ionizing a supersonic hydrogen gas jet using 2-ps, high-power (sub-terawatt) CO_2 laser pulses (38) (see *Methods*). The magnetic fields in the plasma and their spatiotemporal evolution were probed by ultrashort relativistic electron bunches delivered by the ATF linear accelerator (39). A set of permanent magnet quadrupoles [PMQs (40, 41)] were used to relay and magnify the electron probe to a scintillator screen which converted the modulated electron flux to an optical image. With the movable PMQs inserted, the image was magnified by 3.4× (further magnified by the optical system to an overall magnification of ~7.8×) with a spatial resolution of 2.9 μm.

By changing the delay of the electron probe with respect to the CO_2 laser, a movie of the density bunching of the electron beam due to its deflections by the magnetic field in the plasma was made (see Supplemental Information). In Fig. 1*B*, we show the raw data of the density modulations on the electron beam at representative times with respect to the plasma formation. The total time interval covered by these frames is ~150 ps. The images were obtained with PMQs inserted, with their object plane 10 ± 0.5 mm downstream of the plasma. The time zero was defined when the observable structures within the electron beam reached roughly the center of the field of view. In the next frame (3.3 ps later), the front of the structure moved toward the right by ~1 mm as expected. The jitter between the laser and the electron probe was determined to be ~0.4 ps (see *SI Appendix*, Fig. S1 Supplemental Information).

We argue that the observed structures in the probe electron beam are caused by Weibel-generated magnetic fields in the plasma. In the experiment, the electron probe was orthogonal to the CO_2 laser pulse, i.e., in the positive z direction in Fig. 1*A*. Because of this probing geometry, the probe was deflected by the B_x and B_y components by the $\boldsymbol{v} \times \mathbf{B}$ force, not B_z. The contributions of small-amplitude wakes, stimulated Raman back scattering generated plasma waves (42), and other stochastic electric fields in the plasma are negligible because these fields oscillate at plasma frequency ω_p and therefore will be averaged over many periods ($\omega_p^{-1} \approx 13$ fs for $n_e = 1.8 \times 10^{18}\,{\rm cm}^{-3}$) as the picosecond long probe traverses the plasma (43, 44). In the 3.3 ps frame, the most prominent features

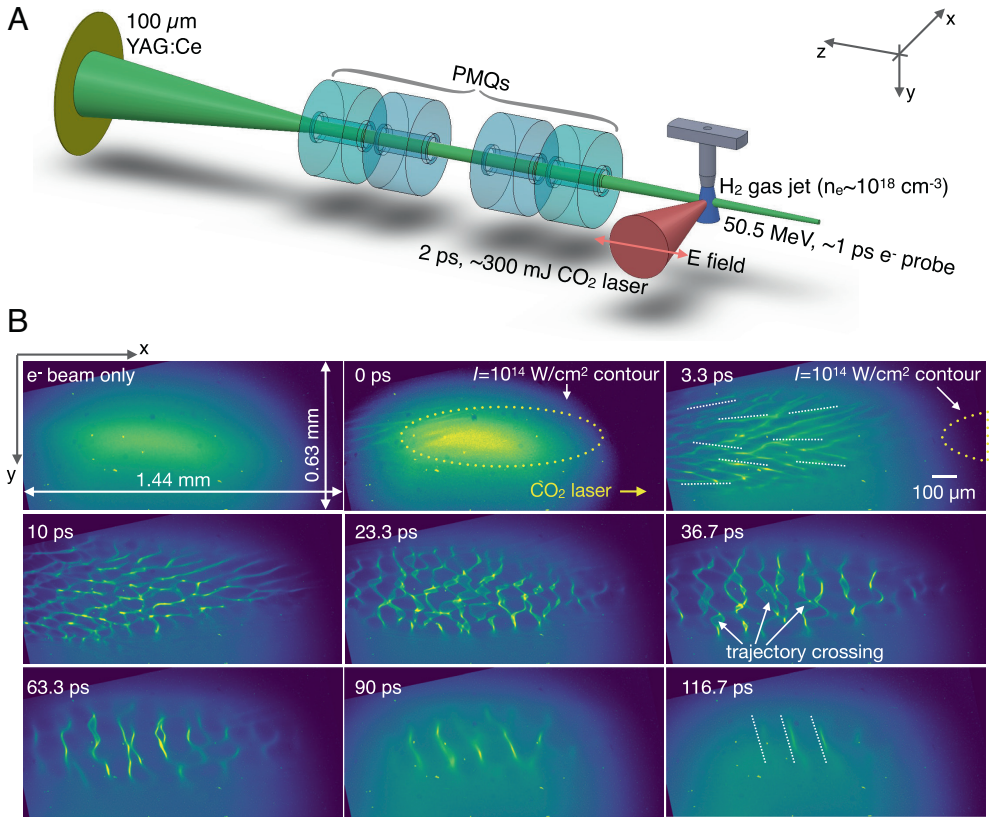

Fig. 1. Experimental setup and representative snapshots of self-generated Weibel magnetic fields. (*A*) Sketch of the experimental layout. (*B*) Representative frames from the movie of the electron beam deflection by fields in the plasma. The first frame shows the e^- beam profile with no laser. The following frames show the evolution of the self-generated fields in the plasma. The yellow dotted ellipse on the 0 ps frame outlines the estimated 10^{14} W/cm^2 (ionization threshold) intensity contour of the CO_2 laser. The dotted white lines on the 3.3 ps and 116.7 ps frames are added to highlight the orientation of selected density strips. On the 36.7 ps frame, the white arrows mark structures caused by the trajectory crossing of the probe electrons which shift the effective object plane closer to the plasma. All images were rotated counterclockwise by 12° to correct the PMQ-induced slant and put the longer dimension of the elliptical plasma parallel to the laser propagation direction.

seen are density strips within the electron beam that are approximately parallel to the laser propagation direction (see the dotted white lines in Fig. 1*B*). We will see in the next section that these electron density modulations can be transformed into magnetic fields and plasma current density maps. These horizontal density strips must arise because the probe electrons are deflected in the vertical (y) direction, which implies that within this period the dominant component of the magnetic field is B_x with its wavevector along the y direction. At this time, the CO_2 laser pulse has fully traversed the region probed by the electron beam, and the density structures have appeared in at least 2/3 of the frame. The evolution of the density structures in the xy plane is seen in the back of the frame. The 10-ps frame is particularly interesting as it clearly shows that these initially predominantly horizontal strips (the rightmost side of the frame) start to break up in the xy plane into smaller-scale "fish-net" structures on the left-hand side within ~1 ps. These fish-net structures are in sharp focus in the 10-ps frame, which is indicative of deflected electrons coming to a focus at the object plane of the PMQs. A fish-net structure means that the electrons are bent in both directions (x and y) and that the two components B_x and B_y have approximately equal magnitude. The magnetic fields continue to grow, moving the object plane closer to the plasma, causing trajectory crossing of the probe electrons before they reach the object plane of the PMQs and blurring the structures as seen in the 23.3 ps frame. These fish-net structures last for approximately 20 ps. In the next frame (36.7 ps), the density strips begin to line up in the vertical direction, which indicates that the electrons are now predominantly deflected along the horizontal (x) direction by the B_y component. As the instability continues to evolve, the density strips remain along the vertical direction, but the spacing between the strips keeps increasing and the structure appears to become a quasi-single mode. In the last frame (116.7 ps), the field has evolved to a quasi-single mode with a wavelength of ~145 μm (see dotted white lines). In addition to this morphological change, the magnitude of the electron probe density modulation also evolves as a function of time, which correlates with the evolution of the magnetic field amplitude.

Retrieved Magnetic Fields and Current Density Distribution. The path integrals of the magnetic fields along the probe propagation direction were retrieved by solving an equivalent optimal transport problem (45) (see *Methods*). The retrieved $\int B_x dz$ and $\int B_y dz$ fields for a representative frame (the 10-ps frame in Fig. 1*B*) are shown in Fig. 2 *A* and *B*, respectively. The calculated path-integrated magnetic fields have a peak magnitude of ~100 Tesla × μm. For simplicity, the plasma was approximated as a slab (rather than the more realistic cylindrical plasma) with a thickness of 300 μm inferred from the transverse extent in the vertical direction. The retrieved path-integrated B_x and B_y fields have similar peak magnitudes of ~0.35 Tesla. Implications of violating this assumption are discussed later.

The measured magnetic fields are predominantly generated by the quasi-static plasma currents, i.e., the contribution of the displacement current is small. Since the plasma temperature was the highest in the z direction (see the *Simulation* section), we anticipate that J_z is the dominating source for the observed magnetic fields.

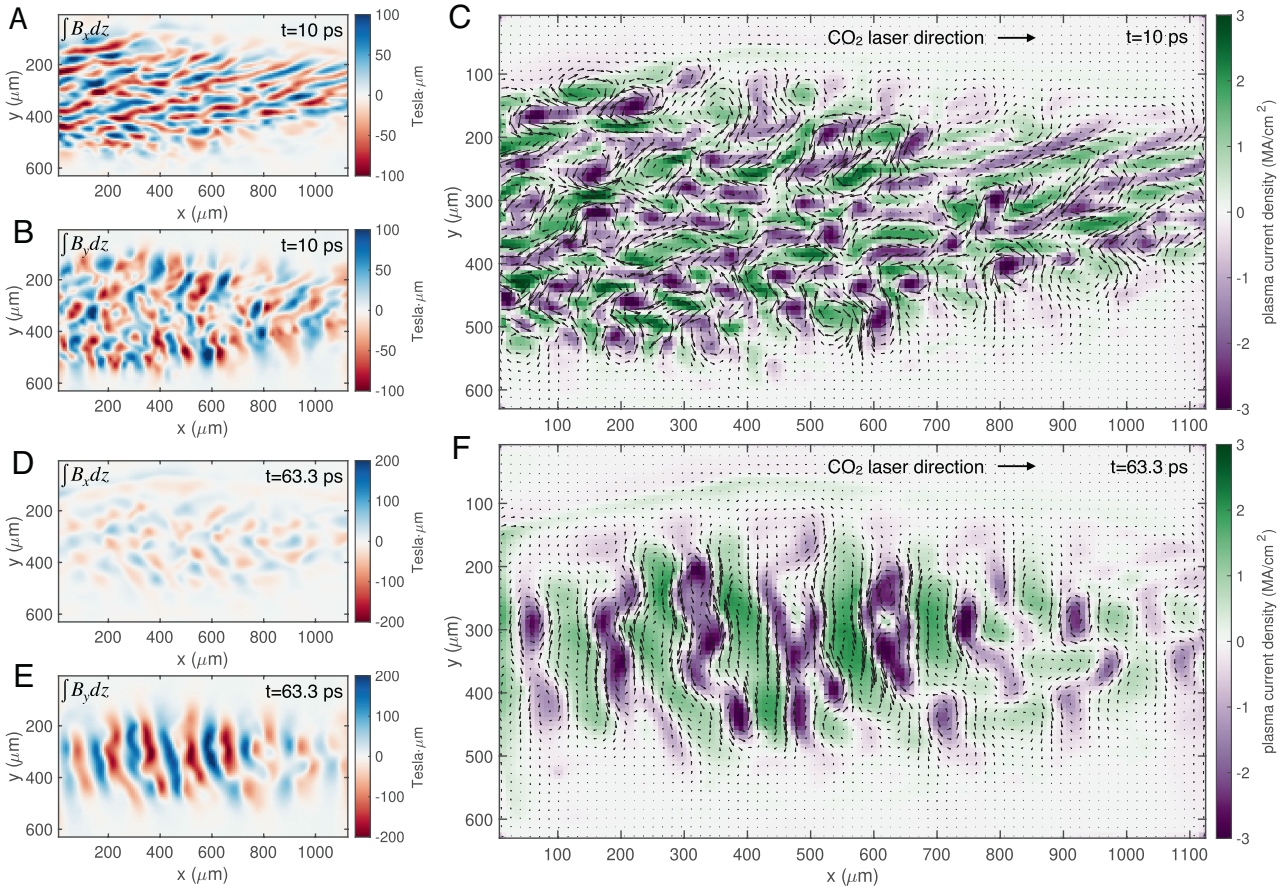

Fig. 2. Retrieved magnetic fields and current density maps. (*A* and *B*) show $\int B_x dz$ and $\int B_y dz$, respectively, for the 10 ps frame. The current density calculated using these magnetic fields is shown in (*C*) by the color scale, whereas the arrows show the vector magnetic field $\mathbf{B}_\perp = \hat{x}B_x + \hat{y}B_y$. The corresponding results for the 63.3 ps frame are shown in (*D*–*F*).

Therefore, we calculate the current density J_z using the retrieved two orthogonal magnetic field components by solving Maxwell's curl $\mathbf{H}$ equation (Ampere's law), $J_z = \mu_0^{-1}(\partial_x B_y - \partial_y B_x)$. The calculated 2D distribution of J_z is shown in Fig. 2*C* by the color scale. The plasma current density is modulated along both x and y directions, which supports the multidimensional nature of the instability.

The plasma currents keep merging as the instability grows. To highlight this, the magnetic fields and current density for the 63 ps frame are plotted in Fig. 2 *D*–*F*. At this stage, the instability has saturated and the B_y field dominates over B_x (Fig. 2 *D* and *E*). Additionally, both the size of the current filaments and the spacing between them have increased. The morphology of the current distribution has changed from a 2D fish-net structure to a 1D periodic distribution along the x direction, which is consistent with the B_y field and the observed vertical density strips shown in Figs. 2*E* and 1*B*, respectively.

Using the retrieved current density, we can estimate the magnitude of the plasma current density modulation. Consider a plasma with Maxwellian electron velocity distribution (EVD) along the z direction. It contains an equal number of electrons moving along opposing directions (e.g., $\pm z$). The initially unperturbed plasma current densities are $J_\pm(x) = \pm J_0$ where $J_0 = -en_e\langle v_{+z}\rangle = -en_e v_{th}/\sqrt{2\pi}$ and is uniform on a spatial scale larger than the Debye length. Therefore, without modulation, the net current density $J_z = J_+ + J_-$ is zero everywhere. The growth of Weibel instability causes coalescence of the microscopic plasma currents and leads to the spatial modulation of the current density, which can be assumed as $J_\pm = \pm J_0(1 \pm \frac{\epsilon}{2}\sin kx)$. Here, $\epsilon/2$ and k are the magnitude and wavevector of the modulation for $J_\pm$, respectively. This gives a net current density distribution of $J_z = J_0\,\epsilon \sin kx$. Using the experimental plasma density $n_e = (1.8 \pm 0.2) \times 10^{18}$ cm^{-3} and $T_z \approx 150$ eV from the 3D PIC simulation (see the *Simulation* section), the magnitude of the net current density is calculated to be 59ϵ MA/cm^2. The measured peak magnitude of J_z is about 3 MA/cm^2 (Fig. 2 *C* and *F*), which corresponds to a modulation magnitude of $\epsilon \approx 5\%$. Note that in Weibel's theory, this current density modulation is caused by redistribution of the microscopic plasma currents and does not require plasma density modulation. Nevertheless, density modulation may emerge in the nonlinear stage of the instability (46). We note that in a recent experiment, a current density modulation approaching unity in ion current filaments was measured using optical Thomson scattering (47).

The plasma beta is defined as $\beta \equiv \frac{p_{\rm th}}{p_{\rm mag}}$ where $p_{\rm th} = nk_B T$ is the thermal pressure of the plasma and $p_{\rm mag} = B^2/2\mu_0$ is the magnetic pressure. For $k_B T \approx 150$ eV, $n_e = 1.8 \times 10^{18}$ cm^{-3}, and the measured $\langle B^2\rangle^{1/2} \approx 0.35$ Tesla, these pressures are calculated as $p_{\rm th} \approx 430$ bar and $p_{\rm mag} \approx 0.5$ bar. Therefore, the plasma beta is $\beta \approx 860$. We note that this number represents the upper limit of the plasma beta in the experiment due to two reasons. First, there are structures indicating probe trajectory crossing after 23 ps (Fig. 1*B*), which will reduce the retrieved magnitude of the magnetic field. In other words, the actual magnetic field strength is

larger than the deduced one, by an estimated factor of ~2 which will reduce the β by a factor of 4. Second, the B field may not be uniform across the whole plasma along the probe propagation direction as assumed, namely, $B = \langle B \rangle + \delta B$, where $\langle B \rangle$ represents the average of B. The variation δB leads to $\langle B^2 \rangle = \langle B \rangle^2 + \langle \delta B^2 \rangle = 2\langle B \rangle^2$ if we assume $\delta B \sim \langle B \rangle$. This means the actual plasma beta is two times smaller than that evaluated using $\langle B \rangle$. Taking both factors into account, the plasma beta may be reduced to ~ 100. This means that upon saturation, about 1% of the thermal energy in the plasma is converted to the magnetic field energy, which is on the same order (~4%) as observed in previous 3D PIC simulations with much hotter temperatures ($T_\perp = 16$ keV and $T_\parallel = 0.64$ keV) (23). Similar level of energy conversion was also observed in PIC simulations of expanding plasmas (48) and anisotropic plasmas driven by shearing flows (49), and the authors suggest that conversion of percent level of thermal energy into magnetic field energy via the Weibel instability may be sufficient for seeding the galactic dynamo (50, 51).

2D *k*-Spectrum Evolution of the Magnetic Fields. As previously explained, the Weibel instability starts growing with many different wavelengths, and thus a *k*-resolved analysis is necessary for understanding the instability evolution. In Fig. 3, we show the 2D *k*-spectrum of the retrieved magnetic fields (B_x, Fig. 3 *A*, and B_y, Fig. 3*B*). Here, each *k*-spectrum was obtained by taking the 2D Fourier transform of the retrieved magnetic fields. These results highlight the evolution of the unstable modes and the transition to the dominating wavevector in the 2D *k*-space. For instance, we can see that both the B_x and B_y components start growing with a broad spectrum and then the unstable region continuously shrinks in size and eventually narrow peaks appear which corresponds to quasi-single mode formation (marked by the white circles and arrows). For instance, in the last two frames (90 and 116.7 ps) of the B_y spectra, a narrow peak with $\frac{k_x}{2\pi} \approx 0.007\ \mu\text{m}^{-1}$ which corresponds to a structure with a wavelength of $\lambda_x \approx 145 \pm 20\ \mu$m and $\frac{k_y}{2\pi} \approx 0$ has formed.

The temporal evolution of the B_x and B_y spectra is plotted in Fig. 3 *C* and *D*, respectively. The B_x component begins with a spectral peak at $\lambda_y \approx 50\ \mu$m immediately following the onset of the instability (at 3.3 ps) that continuously shifts toward smaller k_y or increasing wavelength. For instance, the wavelength of B_x has increased to ~250 μm at ~50 ps and remains almost unchanged after that. This may be because the plasma is bounded in the transverse direction and therefore sets an upper limit for the wavelength. The B_y field also starts with a broad spectrum following the onset of the instability, but its wavelength converges to ~145 μm at ~30 ps and remains almost unchanged for up to ~100 ps. We note that, however, in the experiment the wavelength of the B_y field did continue increasing with time and reached ~300 μm at ~0.5 ns.

From the *k*- and time-resolved data shown in Fig. 3 *C* and *D*, we can deduce the *k*-resolved growth rates of the two magnetic field components. For instance, each row in Fig. 3*C* represents the temporal evolution of a specific k_y component of the measured B_x field and, therefore, the *k*-resolved growth rate is deduced by assuming an exponential growth and fitting the data (using the 0–3.3 ps data when the field grows most rapidly, see *SI Appendix*). The result is shown by the blue curve in Fig. 3*E*. The growth rate peaks at $k_x \approx 0.5\omega_p c^{-1}$. Because the probe electron density modulation caused by the B_x field appears as strips along the horizontal direction, which is equivalent to the time axis, it is also possible to estimate the growth rate using a single frame (e.g., the 3.3 ps frame in Fig. 1*B*) by tracking the increase of density modulation magnitude of each column from right to left, which corresponds to an increasing delay (see *SI Appendix*). The growth rate deduced from the density modulation is shown by the green curve in Fig. 3*E*. The two methods qualitatively agree with each other and the latter intraframe method gives a slightly larger growth rate due to higher temporal resolution. A similar analysis is applied to the B_y field and the result is shown by the orange curve in Fig. 3*F*.

Using the tri-Maxwellian EVD obtained from PIC simulation, we can calculate the growth rate $\gamma(k)$ for the two magnetic field components that are perpendicular to the probe direction assuming no coupling between them in the linear phase (1D theory for each component, see *Methods*). The calculation results are shown by the red dashed lines in Fig. 3 *E* and *F*. Reasonable agreement is seen for both field components, further supporting the argument that these fields are associated with the Weibel instability.

PIC Simulation Results. In this section, we present simulation results that qualitatively reproduce our experimental observations. The simulation was done using the Osiris 4.0 code (52), and it included both the ionization process and the subsequent multidimensional self-consistent evolution of the plasma. The details of the simulation setup can be found in the *Methods* section.

The simulation results are summarized in Fig. 4. In Fig. 4*A*, we show the distribution of electrons in the 3D momentum space right after the laser has passed. The EVDs in each direction are plotted in Fig. 4*B*. In all the three directions, the EVDs can be well fitted by a Maxwellian distribution. As expected, the plasma temperature in the laser polarization (z) direction is the highest ($T_z \approx 150$ eV). The temperature in the y direction is the lowest ($T_y \approx 30$ eV), whereas the temperature in the laser propagation direction is higher ($T_x \approx 80$ eV). We note that if only the ionization process is considered, T_x and T_y should be similar. The increased T_x indicates that the plasma has been preferentially heated in the longitudinal direction. Plasmas with such temperature anisotropy are unstable to Weibel instability as we have observed in the experiment. These temperatures and the corresponding anisotropies $A_{zy} = \frac{T_z}{T_y} - 1 \approx 4$ and $A_{zx} = \frac{T_z}{T_x} - 1 \approx 0.9$ were used to estimate the thermal energy density of the plasma and calculate the Weibel growth rate shown in Fig. 3 *E* and *F*.

The path integrals of the magnetic field components B_x and B_y are shown in Fig. 4 *C* and *D*, respectively. Note that unlike in the experiment, here the integrations were taken by freezing the fields at an instantaneous time. Using these fields, a synthetic probe image was constructed and is shown in Fig. 4*E*. The image reproduces the observed qualitative features of the net structure (see the 10 ps frame in Fig. 1*B*). Several representative 2D *k*-spectra of the path-integrated magnetic fields ($\int B_x dz$ and $\int B_y dz$) are shown in Fig. 4 *F* and *G*, respectively. As do the experimental plots shown in Fig. 3 *A* and *B*, these plots also show the continuous narrowing of the initially broad 2D *k*-spectrum and the formation of a quasi-single mode at later times. The complete temporal evolution of the k_y component of B_x is shown in Fig. 4*H* and a similar plot for $B_y(k_x)$ is depicted in Fig. 4*I*. The key features observed in the experiment, including the transition to the dominant wavenumber in the 2D *k*-space and the narrowing of both the k_y- and k_x-spectra as a function of time, are also qualitatively reproduced. Simulation shows that the root mean square (RMS) magnitude of the magnetic field reaches a peak of ~0.4 Tesla which qualitatively agrees with that observed in the experiment and corresponds to about 0.9% of the thermal energy. Apart from these agreements, the instability seems to evolve about three times faster than that in the experiment. One possible reason is artificial numerical

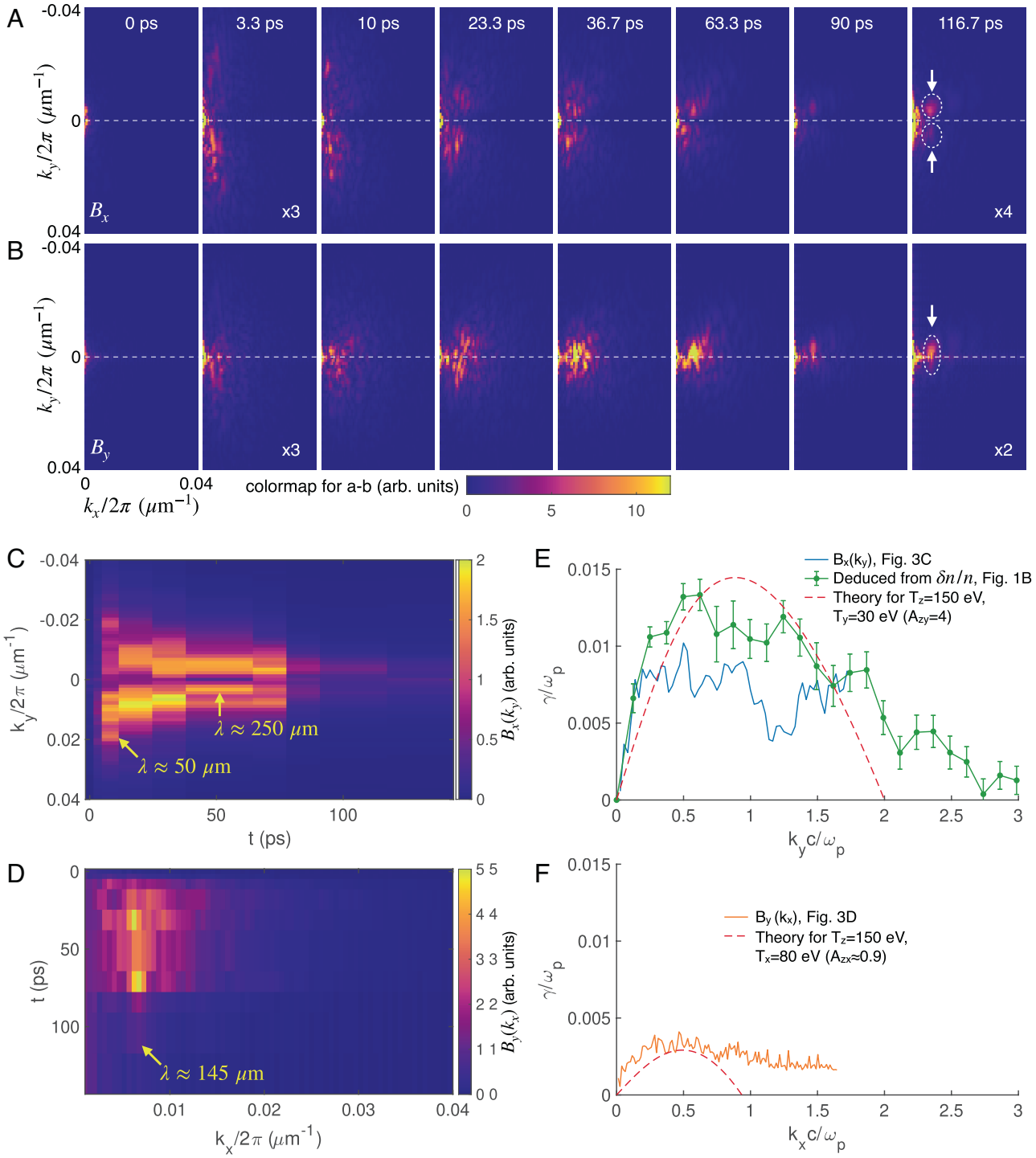

Fig. 3. *k*-spectrum evolution of the retrieved magnetic fields from the experimental data. (*A* and *B*) Evolution of the 2D *k*-spectrum for B_x and B_y, respectively. The color scale for each frame is the same. The white circles and arrows mark the surviving quasi-single mode in the last frame. (*C*) Temporal evolution of the k_y component of B_x (averaged over $\frac{k_x}{2\pi} \in [0.002, 0.02]$ μm^{-1}). The yellow arrow marks the dominant mode at different delays. (*D*) Evolution of the k_x component of B_y (averaged over $\frac{k_y}{2\pi} \in [-0.02, 0.02]$ μm^{-1}). The yellow arrow marks the wavelength of the surviving quasi-single mode. (*E* and *F*) *k*-resolved growth rates and comparison with 1D kinetic theory. The blue curve in (*E*) shows the growth rate deduced using the data in (*C*) and the green curve is deduced from the probe density modulation directly (the 3.3 ps frame in Fig. 1*B*). The orange curve in (*F*) is deduced using the data in (*D*). The dashed lines in (*E* and *F*) show the kinetic theory predictions.

collisions caused by only eight particles per cell to save simulation time. Increasing number of particles per cell can suppress the numerical collisions. We have performed a series of 2D simulations with number of particles per cell up to 1,024, and the results show that the magnetic fields reach saturation at ~50 ps and last for over 100 ps, which agree better with the experimental observations.

Discussion

We have shown that the electron Weibel instability can self-generate quasistatic magnetic fields in plasmas with temperature anisotropy induced by optical-field ionization by picosecond intense CO_2 laser pulses. The time-resolved measurements indicate that the magnetic field magnitude and spectrum evolve on a time scale

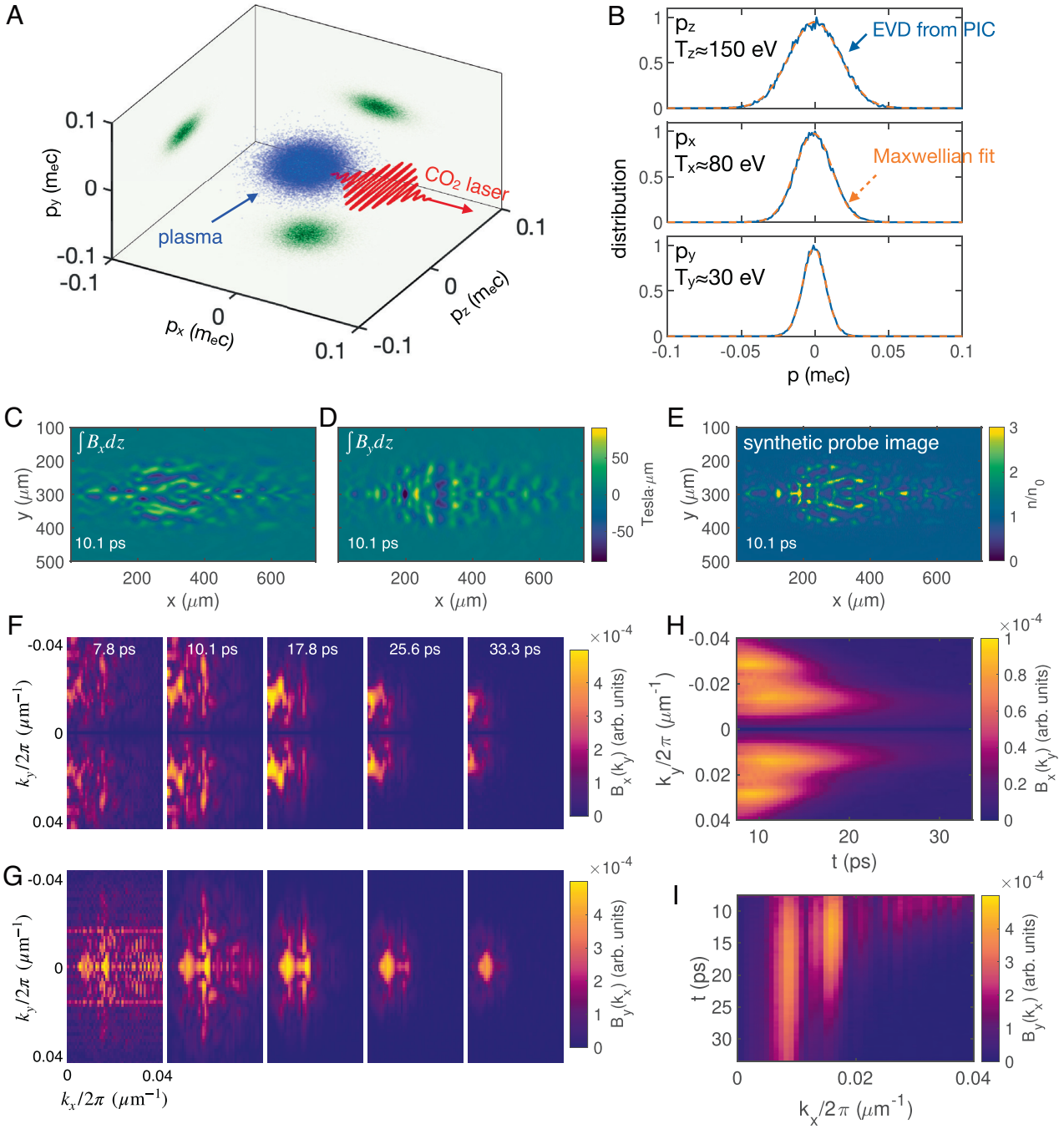

Fig. 4. Self-consistent 3D PIC simulation results. (*A*) Simulated distribution of OFI plasma electrons in the 3D momentum space. (*B*) Projected EVDs (blue) and Maxwellian fits (red). In all the three cases, the R-squared values are larger than 0.997. See *SI Appendix*, Fig. S2 for the fitting residuals. (*C* and *D*) show the path integrals of B_x and B_y obtained from the simulation, respectively. (*E*) is a synthetic probe image using the experimental parameters. (*F* and *G*) show the evolution of the 2D *k*-spectrum for path integrals of B_x and B_y, respectively. (*H* and *I*) show the temporal evolution of the k_y component of B_x (averaged over $0.01 < k_x / 2\pi(\mu m^{-1}) < 0.04$) and the k_x component of B_y (averaged over $-0.01 < k_y / 2\pi(\mu m^{-1}) < 0.01$), respectively.

of tens of ps, which implies that the electron velocity distributions also evolve toward a thermal plasma on a similar time scale. Although the Weibel instability is thought to be purely electromagnetic, in the nonlinear stage, ion motion may lead to density fluctuations that need to be measured using optical Thomson scattering.

The actual EVDs of the plasma in this experiment are anisotropic in all the three dimensions, which give rise to complex Weibel magnetic field structures. We have probed the fields along one direction and hence in the *xy* plane. To get a complete characterization of the 3D distribution of the magnetic field, electron probing at multiple angles is necessary. A practical way for doing this could be rotating the polarization direction of the CO_2 laser.

We note that in these experiments, high field ionization of the hydrogen gas using a long-wavelength CO_2 laser produced a large initial temperature anisotropy. Despite the relatively high plasma density, the Weibel magnetic fields grow before the collisionless collective effects (kinetic) together with collisions can isotropize the plasma. As for astrophysical plasmas, we know little about the details of the electron distribution function and whether, over the vast distances of the galactic plasma [O(Mpc)], it is sufficiently anisotropic to initiate the electron Weibel instability. This issue

needs further work. Another issue is the possible thermalization of the electrons before the seed magnetic field is produced by the Weibel instability. The estimates of this collisional thermalization process are made difficult by the extremely tenuous nature and complex composition of the galactic plasma. However, recent simulations have suggested that temperature anisotropy can also be self-consistently induced due to Biermann battery effect (53) or under the action of large-scale flows (49). This relaxes the requirement on the initial temperature anisotropy to be large so that the thermal Weibel magnetic fields can grow despite thermalizing collisions, making it a candidate for the seed magnetic field on cosmological scales.

In summary, we have presented an unambiguous existence proof of the electron Weibel magnetic fields driven by a large effective temperature anisotropy as originally envisioned by Weibel. From these measurements, we have retrieved the 2D distribution of the magnetic fields and plasma current density and deduced the ultrafast dynamics of the fields and current density including the evolution of their 2D k-spectra and the k-resolved growth rate, which agree with kinetic theory predictions and PIC simulations. We observed the formation of a quasi-single mode of the magnetic field after the instability saturates which can last for up to half a nanosecond. Upon saturation, the current density modulation magnitude reaches ~5% and about 1% of the thermal energy of the plasma is converted to the magnetic field energy. These results represent a significant advance of the experimental understanding of Weibel instability. In our opinion, the OFI platform used here has a great potential for exploring ultrafast magnetic field dynamics in relativistic, anisotropic plasmas produced by ionization of high Z atoms in the laboratory relevant to astrophysical plasmas.

Materials and Methods

Experimental Setup. The experiment was carried out at the ATF-BNL. The high-power CO_2 laser system is capable of delivering up to 5 TW power within a pulse duration of about 2 ps (full width at half maxima) (38). For the data presented here, the laser energy was kept at a few hundred mJ such that the laser was able to fully ionize the hydrogen gas jet without driving large-amplitude self-modulated wakes. The laser was focused by an F/2 off-axis parabola with a 3-mm hole and the focal spot size was measured to be $w_0 \approx 45$ μm in vacuum. To enlarge the transverse extent of the plasma, the gas jet was shifted toward the upstream of the laser (closer to the off-axis parabola) by about 2 mm. At this location, the laser spot size was calculated to be $w \approx 140$ μm. The laser was linearly polarized in the horizontal plane with its electric field pointing along the electron probe direction. The plasma was produced by ionizing a supersonic hydrogen gas jet emanating from a converging–diverging nozzle with an opening diameter of 5 mm. The laser beam axis was placed ~2.5 mm above the nozzle exit. For the data presented here, the backing pressure of the nozzle was ~87 psig. The neutral density profile of the gas jet was measured offline using our recently developed ionization-induced plasma grating method (54) (see *SI Appendix*, Fig. S6). The peak plasma density, assuming that the gas jet is fully ionized by the CO_2 laser, is $(1.8 \pm 0.2) \times 10^{18} \mathrm{cm}^{-3}$. As they traverse through the plasma, the probe electrons receive transverse deflections by the magnetic fields. Then, the probe propagates in the vacuum and the angular deflection translates into electron flux modulation. A set of PMQs like those used in refs. 40 and 41 was used to relay and magnify the electron probe image to a scintillator screen (100-μm thick YAG: Ce crystal with both sides polished and one side coated with indium tin oxide) that was placed ~0.5 m away from the plasma. The electron flux distributions were converted to optical images by the scintillator crystal and the latter was further magnified using an objective (Mituyoto 5× Plan APO) and recorded by a charge-coupled device (Basler acA1920-50gm with 5.86 μm pixel size) equipped with a camera lens with remote focus control. The probe electron beam was delivered by the ATF linac at 1.5 Hz but the data were taken at a lower laser repetition rate using a trigger signal to synchronize the gas jet, CO_2 laser, e^- beam, and the camera. The energy of the probe beam was fixed at 50.5 MeV (0.2% energy spread) to match the designed optimal energy for the PMQs. The pulse duration of the probe beam was tuned to be ~1–2 ps by varying the slit size to select a portion of the longer pulse. Although the emittance of the electron beam was not measured during this run, it was estimated to be ~1.4 mm · mrad based on previous measurements (39). The focus of the electron beam was shifted upstream such that the beam was able to cover a few mm field of view.

Electron Imaging System. The key part of the electron imaging system is the PMQs that can relay the electron images at the object plane to the image plane by a 2D one-to-one mapping. The set of PMQs includes four pieces (two identical pairs) of Halbach-type high-gradient quadrupoles arranged in the A-B-B-A order. Two pairs of the PMQs were mounted separately such that the separation between them can be adjusted to change the magnification and move the object plane location. The two assemblies were held by a third motorized translation stage which allows the PMQs to be moved away from the electron beam path. In the PMQ-in configuration, the electron probe formed images at 10 ± 0.5 mm (tunable from 0 to 25 mm) from the plasma, and then the image was relayed and magnified by the PMQs. In the PMQ-out configuration, the electron probe formed images directly on the scintillator screen. In both configurations, the overall magnification and resolving power of the imaging system were calibrated using transmission electron microscope grids. The magnifications were ~7.8× and ~3.7× and the resolving powers were ~2.9 μm and ~10 μm for the two configurations.

Retrieval of Magnetic Fields. To retrieve the magnetic fields, the first step was to solve for the deflection angles α_x and α_y of the probe electrons. Using the measured probe density profile $n(x, y)$, a synthetic background n_0 was estimated by smoothing the image using a code based on a penalized least squares method (55). Then, the relative density modulation was calculated as $n/n_0 - 1$. The algorithm in ref. 45 was used to calculate the optimal transport of a uniform background to the relative density modulation. Before doing the calculation, the region of interest of the image was selected and downsampled by a factor of 10 to reduce its size to 90×150 pixels to reduce the computational resource requirements to an affordable level. Then, the deflection angles were used to calculate the transverse magnetic fields B_x and B_y, with the assumption that the plasma has a slab geometry with a thickness of 300 μm. The current density J_z was calculated using Ampere's law as explained in the main text.

Growth Rate Calculation. The growth rates of the Weibel instability were calculated using 1D kinetic theory. The dispersion relation for the Weibel mode in an anisotropic plasma is (56)

$$1 - \frac{c^2 k^2}{\omega^2} + \frac{\omega_p^2}{\omega^2}\left[A + (A+1)\,\xi Z(\xi)\right] = 0,$$

where $\omega = i\gamma$ is the complex frequency, γ is the growth rate, k is the wavenumber of the magnetic field, $A = \frac{T_{\mathrm{hot}}}{T_{\mathrm{cold}}} - 1$ is the temperature anisotropy, $\xi = \frac{\omega}{\sqrt{2}kv_{\mathrm{hot}}}$, $v_{\mathrm{hot}} = \sqrt{\frac{k_B T_{hot}}{m_e}}$ is the thermal velocity in the hot temperature direction, and $Z(\xi)$ is the plasma dispersion function. The theoretical growth rates in Fig. 3 *E* and *F* were calculated using ($T_z = 150$ eV, $T_y = 30$ eV, $A_{zy} = \frac{T_z}{T_y} - 1 = 4$) and ($T_z = 150$ eV, $T_x = 80$ eV, $A_{zx} = \frac{T_z}{T_x} - 1 = 0.875$), respectively.

PIC Simulation. The 3D PIC simulation was performed using the Osiris 4.0 code (52). The stationary simulation box has dimensions of $500(x) \times 400(y) \times 400(z)\ c/\omega_0$. Here, ω_0 is the frequency of the CO_2 laser ($\lambda = 9.2\ \mu$m). A hydrogen (atomic) gas was initialized inside the box. In the laser propagation direction, the gas density profile contains two $10\ c/\omega_0$ linear ramps on both ends and two $10\ c/\omega_0$ gaps were set between the gas and box boundary. In the other two orthogonal directions, the gas density is uniform. The peak plasma density was set to $10^{18}\ \mathrm{cm}^{-3}$. A linearly polarized laser with the experimental parameters ($\lambda = 9.2\ \mu$m, $\tau = 2$ps, $w_0 = 45\ \mu$m, $E = 115$mJ) was launched from the left wall of the box. The vacuum focal plane of the laser was set to $x = 1,520\ c/\omega_0$, which means that the simulation box covers the region that is ~1.5 mm upstream of the focus to mimic the experimental condition. The ionization of hydrogen was calculated using the Ammosov–Delone–Krainov (ADK)

model (57) and the subsequent evolution of the OFI plasma was self-consistently modeled. The 3D distribution of the magnetic fields and plasma currents were saved every ~0.5 ps for analysis.

Data, Materials, and Software Availability. All study data are included in the article and/or *SI Appendix*.

ACKNOWLEDGMENTS. This work was supported by the U.S. Department of Energy Grant Nos. DE-SC0010064 and DE-SC0014043 as well as NSF Grant No. 2003354. Audrey Farrell would like to acknowledge the support from the NSF GRFP (Grant No. DGE-2034835). The simulations were performed on the NERSC Cori cluster operated under Contract No. DE-AC02-5CH11231 at Lawrence Berkeley National Laboratory (LBNL). We thank Dr. Mark Palmer, Prof. Vladimir Litvinenko, Dr. Marcus Babzien, and the ATF staff for their support and hospitality throughout this work. We also acknowledge Dr. Yu Fang for his help with measuring the PMQs.

Author affiliations: [a]Department of Electrical and Computer Engineering, University of California, Los Angeles, CA 90095; [b]Department of Physics and Astronomy, Stony Brook University, New York, NY 11794; [c]Accelerator Test Facility, Brookhaven National Laboratory, Upton, NY 11973; [d]Institute of Atomic and Molecular Sciences, Academia Sinica, Taipei 10617, Taiwan; [e]Department of Engineering Physics, Tsinghua University, Beijing 100084, China; and [f]Department of Physics and Astronomy, University of California, Los Angeles, CA 90095

1. E. G. Zweibel, C. Heiles, Magnetic fields in galaxies and beyond. *Nature* **385**, 131–136 (1997).
2. L. M. Widrow, Origin of galactic and extragalactic magnetic fields. *Rev. Mod. Phys.* **74**, 775–823 (2002).
3. R. M. Kulsrud, E. G. Zweibel, On the origin of cosmic magnetic fields. *Rep. Prog. Phys.* **71**, 046901 (2008).
4. E. N. Parker, The origin of magnetic fields. *ApJ* **160**, 383 (1970).
5. R. M. Kulsrud, A critical review of galactic dynamos. *Ann. Rev. Astron. Astrophys.* **37**, 37–64 (1999).
6. E. Zweibel, The seeds of a magnetic universe. *Physics* **6**, 85 (2013).
7. L. M. Widrow *et al.*, The first magnetic fields. *Space Sci. Rev.* **166**, 37–70 (2012).
8. S. Naoz, R. Narayan, Generation of primordial magnetic fields on linear overdensity scales. *Phys. Rev. Lett.* **111**, 051303 (2013).
9. G. Gregori *et al.*, Generation of scaled protogalactic seed magnetic fields in laser-produced shock waves. *Nature* **481**, 480–483 (2012).
10. E. S. Weibel, Spontaneously growing transverse waves in a plasma due to an anisotropic velocity distribution. *Phys. Rev. Lett.* **2**, 83–84 (1959).
11. B. D. Fried, Mechanism for instability of transverse plasma waves. *Phys. Fluids* **2**, 337 (1959).
12. M. Lazar, R. Schlickeiser, R. Wielebinski, S. Poedts, Cosmological effects of weibel-type instabilities. *ApJ* **693**, 1133–1141 (2009).
13. R. Schlickeiser, P. K. Shukla, Cosmological magnetic field generation by the weibel instability. *ApJ* **599**, L57–L60 (2003).
14. A. A. Schekochihin, S. C. Cowley, R. M. Kulsrud, G. W. Hammett, P. Sharma, Plasma instabilities and magnetic field growth in clusters of galaxies. *ApJ* **629**, 139–142 (2005).
15. M. V. Medvedev, M. Fiore, R. A. Fonseca, L. O. Silva, W. B. Mori, Long-Time evolution of magnetic fields in relativistic gamma-ray burst shocks. *ApJ* **618**, L75–L78 (2005).
16. L. O. Silva *et al.*, Interpenetrating plasma shells: Near-equipartition magnetic field generation and nonthermal particle acceleration. *ApJ* **596**, L121–L124 (2003).
17. M. V. Medvedev, L. O. Silva, M. Kamionkowski, Cluster magnetic fields from large-scale structure and galaxy cluster shocks. *ApJ* **642**, L1–L4 (2006).
18. W. Fox *et al.*, Filamentation instability of counterstreaming laser-driven plasmas. *Phys. Rev. Lett.* **111**, 225002 (2013).
19. N. L. Kugland *et al.*, Self-organized electromagnetic field structures in laser-produced counter-streaming plasmas. *Nat. Phys.* **8**, 809–812 (2012).
20. C. M. Huntington *et al.*, Observation of magnetic field generation via the Weibel instability in interpenetrating plasma flows. *Nat. Phys.* **11**, 173–176 (2015).
21. A. Bret, L. Gremillet, D. Bénisti, E. Lefebvre, Exact relativistic kinetic theory of an electron-beam–plasma system: Hierarchy of the competing modes in the system-parameter space. *Phys. Rev. Lett.* **100**, 205008 (2008).
22. A. Bret, L. Gremillet, M. E. Dieckmann, Multidimensional electron beam-plasma instabilities in the relativistic regime. *Phys. Plasmas* **17**, 120501 (2010).
23. D. V. Romanov, V. Yu. Bychenkov, W. Rozmus, C. E. Capjack, R. Fedosejevs, Self-organization of a Plasma due to 3D evolution of the Weibel instability. *Phys. Rev. Lett.* **93**, 215004 (2004).
24. C.-K. Huang, C.-J. Zhang, K. A. Marsh, C. E. Clayton, C. Joshi, Initializing anisotropic electron velocity distribution functions in optical-field ionized plasmas. *Plasma Phys. Control. Fusion* **62**, 024011 (2020).
25. C. Zhang *et al.*, Ultrafast optical field–ionized gases–A laboratory platform for studying kinetic plasma instabilities. *Sci. Adv.* **5**, eaax4545 (2019).
26. C. Zhang, C.-K. Huang, K. A. Marsh, C. Joshi, Probing thermal Weibel instability in optical-field-ionized plasmas using relativistic electron bunches. *Plasma Phys. Control. Fusion* **62**, 024010 (2020).
27. C. Zhang *et al.*, Measurements of the growth and saturation of electron Weibel instability in optical-field ionized plasmas. *Phys. Rev. Lett.* **125**, 255001 (2020).
28. F. Fiuza *et al.*, Electron acceleration in laboratory-produced turbulent collisionless shocks. *Nat. Phys.* **16**, 916–920 (2020).
29. B. Allen *et al.*, Experimental study of current filamentation instability. *Phys. Rev. Lett.* **109**, 185007 (2012).
30. C. M. Huntington *et al.*, Current filamentation instability in laser wakefield accelerators. *Phys. Rev. Lett.* **106**, 105001 (2011).
31. S. Mondal *et al.*, Direct observation of turbulent magnetic fields in hot, dense laser produced plasmas. *Proc. Natl. Acad. Sci. U.S.A.* **109**, 8011–8015 (2012).
32. G. Chatterjee *et al.*, Magnetic turbulence in a table-top laser-plasma relevant to astrophysical scenarios. *Nat. Commun.* **8**, 15970 (2017).
33. S. Zhou *et al.*, Self-organized kilotesla magnetic-tube array in an expanding spherical plasma irradiated by khz femtosecond laser pulses. *Phys. Rev. Lett.* **121**, 255002 (2018).
34. A. Benedetti, M. Tamburini, C. H. Keitel, Giant collimated gamma-ray flashes. *Nat. Photon.* **12**, 319–323 (2018).
35. A. Sampath *et al.*, Extremely dense gamma-ray pulses in electron beam-multifoil collisions. *Phys. Rev. Lett.* **126**, 064801 (2021).
36. G. Raj *et al.*, Probing ultrafast magnetic-field generation by current filamentation instability in femtosecond relativistic laser-matter interactions. *Phys. Rev. Res.* **2**, 023123 (2020).
37. P. S. M. Claveria *et al.*, Spatiotemporal dynamics of ultrarelativistic beam-plasma instabilities. arXiv:2106.11625 [physics] (2021). (November 9, 2021).
38. M. N. Polyanskiy, I. V. Pogorelsky, M. Babzien, M. A. Palmer, Demonstration of a 2 ps, 5 TW peak power, long-wave infrared laser based on chirped-pulse amplification with mixed-isotope CO_2 amplifiers. *OSA Continuum* **3**, 459 (2020).
39. I. V. Pogorelsky, I. Ben-Zvi, Brookhaven National Laboratory's Accelerator Test Facility: Research highlights and plans. *Plasma Phys. Control. Fusion* **56**, 084017 (2014).
40. Z. Zhou *et al.*, Demonstration of single-shot high-quality cascaded high-energy-electron radiography using compact imaging lenses based on permanent-magnet quadrupoles. *Phys. Rev. Appl.* **11**, 034068 (2019).
41. Z. Zhou *et al.*, Visualizing the melting processes in ultrashort intense laser triggered gold mesh with high energy electron radiography. *Matter Radiat. Extremes* **4**, 065402 (2019).
42. D. Umstadter, R. Williams, C. Clayton, C. Joshi, Observation of steepening in electron plasma waves driven by stimulated Raman backscattering. *Phys. Rev. Lett.* **59**, 292–295 (1987).
43. C. J. Zhang *et al.*, Capturing relativistic wakefield structures in plasmas using ultrashort high-energy electrons as a probe. *Sci. Rep.* **6**, 29485 (2016).
44. C. J. Zhang *et al.*, Femtosecond probing of plasma wakefields and observation of the plasma wake reversal using a relativistic electron bunch. *Phys. Rev. Lett.* **119**, 064801 (2017).
45. M. F. Kasim *et al.*, Quantitative shadowgraphy and proton radiography for large intensity modulations. *Phys. Rev. E* **95**, 023306 (2017).
46. L. Palodhi, F. Califano, F. Pegoraro, Nonlinear kinetic development of the Weibel instability and the generation of electrostatic coherent structures. *Plasma Phys. Control. Fusion* **51**, 125006 (2009).
47. G. F. Swadling *et al.*, Measurement of kinetic-scale current filamentation dynamics and associated magnetic fields in interpenetrating plasmas. *Phys. Rev. Lett.* **124**, 215001 (2020).
48. K. M. Schoeffler, N. F. Loureiro, R. A. Fonseca, L. O. Silva, Magnetic-field generation and amplification in an expanding plasma. *Phys. Rev. Lett.* **112**, 175001 (2014).
49. M. Zhou, V. Zhdankin, M. W. Kunz, N. F. Loureiro, D. A. Uzdensky, Spontaneous magnetization of collisionless plasma. *Proc. Natl. Acad. Sci. U.S.A.* **119**, e2119831119 (2022).
50. D. Ryu, H. Kang, J. Cho, S. Das, Turbulence and magnetic fields in the large-scale structure of the universe. *Science* **320**, 909–912 (2008).
51. S. Roh, D. Ryu, H. Kang, S. Ha, H. Jang, Turbulence dynamo in the stratified medium of galaxy clusters. *ApJ* **883**, 138 (2019).
52. R. A. Fonseca *et al.*, "OSIRIS: A Three-dimensional, fully relativistic particle in cell code for modeling plasma based accelerators" in *Computational science–ICCS 2002, Lecture Notes in Computer Science*, P. M. A. Sloot, A. G. Hoekstra, C. J. K. Tan, J. J. Dongarra, Eds. (Springer, Berlin Heidelberg, 2002), pp. 342–351.
53. K. M. Schoeffler, N. F. Loureiro, L. O. Silva, Fully kinetic Biermann battery and associated generation of pressure anisotropy. *Phys. Rev. E* **97**, 033204 (2018).
54. C. Zhang *et al.*, Ionization induced plasma grating and its applications in strong-field ionization measurements. *Plasma Phys. Control. Fusion* **63**, 095011 (2021).
55. D. Garcia, Robust smoothing of gridded data in one and higher dimensions with missing values. *Comput. Stat. Data Anal.* **54**, 1167–1178 (2010).
56. R. L. Morse, Numerical simulation of the weibel instability in one and two dimensions. *Phys. Fluids* **14**, 830 (1971).
57. M. V. Ammosov, N. P. Delone, V. P. Krainov, Tunnel ionization of complex atoms and of atomic ions in an alternating electromagnetic field. *Sov. Phys. JETP* **64**, 1191 (1987).